



Shape-dependency activity of nanostructured CeO₂ in the total oxidation of polycyclic aromatic hydrocarbons

Laura Torrente-Murciano^{a,*}, Alexander Gilbank^a, Begoña Puertolas^b, Tomas Garcia^b, Benjamin Solsona^c, David Chadwick^d

^a Department of Chemical Engineering, University of Bath, Bath, BA2 7AY, UK

^b Instituto de Carboquímica (CSIC), Zaragoza, Spain

^c Department d'Enginyeria Química, Universitat de Valencia, Valencia, Spain

^d Department of Chemical Engineering, Imperial College London, London, SW7 2AZ, UK

ARTICLE INFO

Article history:

Received 27 August 2012

Received in revised form 23 October 2012

Accepted 29 October 2012

Available online 20 November 2012

Keywords:

Ceria

Nanotubes

Nanorods

Nanocubes

Nanostructures

Catalytic total oxidation

VOC

Naphthalene

Morphological diagram

ABSTRACT

A morphological phase diagram is determined to relate the effect of base concentration and temperature during the hydrothermal synthesis with the final ceria nanostructured morphology. Representative samples of nanoparticles, nanorods and nanocubes have been characterized by XRD, N₂ adsorption, TEM, XPS and Raman and catalytically tested for the total oxidation of naphthalene as a model polycyclic aromatic hydrocarbon. Ceria nanoparticles present the highest surface area and smallest crystalline size, leading to the most active of these structures. However if the catalytic activity is normalized by unit of surface area, the observed reactivity trend (nanorods < nanocubes < nanoparticles) is directly related to the concentration of surface oxygen vacancies as a result of the exposure of the (1 1 0) and (1 0 0) preferential planes.

© 2012 Elsevier B.V. All rights reserved.

1. Introduction

Ceria is a well-known rare earth material which presents a highly desirable combination of chemical and physical properties [1]. It has a high oxygen storage capacity (OSC) and high ion conductivity, a high dielectric constant and it shows high transparency in the visible and near IR regions while being a highly efficient UV absorber. As a consequence, it is used in a wide range of applications such as electrochemistry [2], optics [3], and fuel cells [4]. A major application is in the field of catalysis, either as a catalyst itself or as a catalyst support, where its main use is as a component in the three-way catalytic system to reduce automobile exhaust gases [5]. In many of these catalytic applications, a shape-dependency activity of ceria has been observed [6] likely due to the selective exposition of surface planes, being the (1 0 0) surface catalytically more active than the (1 1 1) and (1 1 0) surfaces [7]. Surface plane exposure can be gained by controlling the morphology at the nanoscale, as a way of enhancing the catalytic activity and redox properties at

the same time as the surface area is increased [8]. As an example, the dominated surface plane of morphologies such as nanocubes or nanorods is (1 0 0) which make them more active for CO oxidation than conventional ceria [9].

Consequently, different approaches have been followed to synthesize CeO₂ nanostructures including the use of templates [10], complexing agents [6], electrochemical deposition [11], sol–gel method [12], precipitation followed by ageing [13], hydrothermally using mineralizer agents [14]. Among these, the hydrothermal synthesis is considered the simplest, additive-free and economic method. However, the establishment of a robust and normalized hydrothermal manufacturing method remains elusive and a major challenge lies in the controlled manipulation of the nano-morphology in order to carefully tune its properties. Base concentration and temperature treatment have been found to be key parameters determining the final nano-morphology [9,15] during the hydrothermal synthesis. Additionally, the variety of set-ups and even conditions used for the hydrothermal syntheses, often with adventitious temperature inhomogeneities, leads to difficulties in relating defined conditions to morphological structure.

In recent years, nanocrystalline ceria has been identified as one of the most active catalysts for the total oxidation of a polycyclic

* Corresponding author.

E-mail address: ltm20@bath.ac.uk (L. Torrente-Murciano).

aromatic hydrocarbon (PAH) [16]. PAHs are known to be carcinogenic and are associated with a number of other serious health hazards [17,18]. Therefore, it is important that convenient, practical and cost effective methods are developed for atmospheric PAH abatement. Previous studies have focused on the influence of the ceria nanoparticles' preparation variables, with the aim of determining which catalyst features are required for naphthalene total oxidation as PAH model compound. Factors such as crystallite size, surface area and oxygen defect concentration have been identified as key parameters [19,20]. However, there is no available information in the literature related to the presence of preferential surface planes which can promote the catalytic activity for naphthalene removal.

In this paper, we report on the determination of a morphological phase diagram which relates the effect of base concentration and temperature of the hydrothermal treatment with the final CeO_2 nanostructured morphology. Representative shapes (nanoparticles, nanorods and nanocubes) have been tested for naphthalene total oxidation in order to correlate the physico-chemical properties of ceria with its catalytic oxidation activity.

2. Experimental

2.1. Synthesis and characterization of materials

The standard hydrothermal method was based on that previously reported [9]. 0.6 g of $\text{Ce}(\text{NO}_3)_3 \cdot 6\text{H}_2\text{O}$ were added to a 40 mL NaOH solution in the range of 1–15 M and stirred magnetically for 10 min in a PTFE beaker. The solution was placed in a 45 mL Teflon lined autoclave inside an air-circulating oven which allows gradientless temperature to be achieved throughout the autoclave. The temperature range studied is 70–180 °C at a set synthesis time of 10 h. Following hydrothermal synthesis, the autoclave was allowed to cool to ambient temperature. The powder obtained was filtered, washed several times with deionised water and dried at 120 °C overnight. Large particles of agglomerated dry powder were broken in a mortar prior to further investigation. The phase identification of the samples was done by X-ray diffraction (XRD) analyses using an X'Pert PRO diffractometer by PANalytical with a $\text{Cu K}\alpha$ radiation, operated at 40 kV and 40 mA. Low temperature nitrogen adsorption measurements at 77 K were done using a Micromeritics ASAP 2020 apparatus. Specific surface area was calculated by the BET method (associated error of $\pm 0.5\%$) and pore size distributions were calculated from the desorption data using the BJH model. Samples were degassed at 150 °C prior to analysis to calculate specific surface area. A JEOL 2010 microscope was used for transmission electron images and a JSM6400 microscope for scanning electron images. X-ray photoelectron spectroscopy (XPS) measurements were made on an Omicron ESCA+ photoelectron spectrometer using a non-monochromatized $\text{MgK}\alpha$ X-ray source ($h\nu = 1253.6 \text{ eV}$). Analyser pass energy of 50 eV was used for survey scans and 20 eV for detailed scans. Binding energies are referenced to the $\text{C}1\text{s}$ peak from adventitious carbonaceous contamination, assumed to have a binding energy of 284.5 eV. XPS data were analyzed using CasaXPS software. Shirley background subtraction was applied to all the raw data. All the peaks of the corrected spectra were fitted with a Gaussian–Lorentzian shape function to peak fit the data. Iterations were performed using the Marquardt method. Standard deviations were always lower than 1.5%.

2.2. VOC catalytic oxidation

Catalytic activity tests for naphthalene oxidation were carried out in a fixed bed laboratory micro-reactor. Blank tests were conducted by passing naphthalene (450 vppm) through an

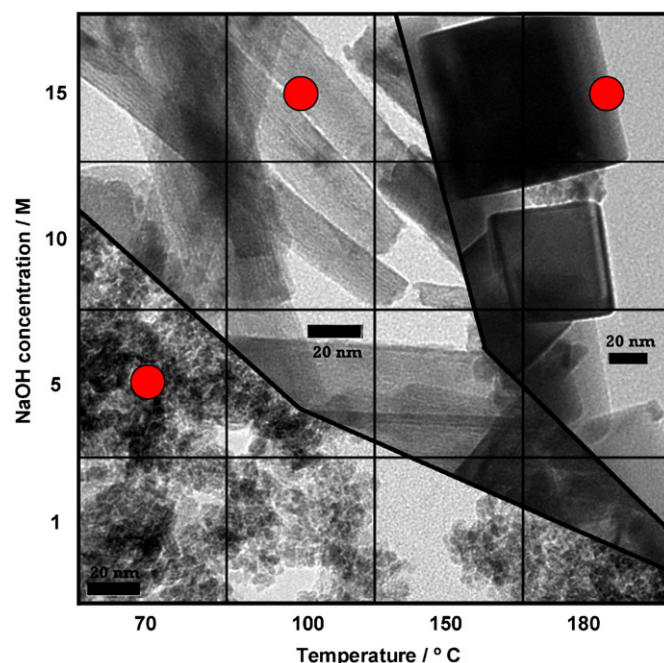


Fig. 1. Morphological phase diagram of CeO_2 after 10 h of hydrothermal treatment. Phase boundaries shown do not imply sharp transitions to pure phases. Circles show the conditions of the representative samples of each morphology taken for the catalytic study.

empty reactor that was heated from 100 °C to 350 °C at a rate of $10^\circ\text{C min}^{-1}$ showing no conversion. Catalysts (pelletized to 0.1–0.2 mm particle size without any binder) were tested using a 3/8" o.d. quartz tube as the reactor. The reaction feed consisted in all cases of ca. 450 vppm naphthalene in a mixture of 20 vol.% oxygen and 80 vol.% helium. A total flow rate of 50 ml min^{-1} was used and the catalysts occupied a constant volume, giving a GHSV of ca. 25,000 h^{-1} for all the catalysts. Analyses were performed by an on-line gas chromatograph with thermal conductivity and flame ionization detectors. The catalytic activity was measured over the temperature range of 100–275 °C, in incremental steps of 25 °C, and temperatures were controlled by a thermocouple, placed in the catalyst bed. Data were obtained at each temperature after the naphthalene adsorption equilibrium was accomplished and steady state activity attained. Four consistent analyses were made at each temperature and average values were calculated. The reaction temperature was increased and the same procedure followed to determine each data point. Oxidation activity was expressed as a yield of carbon dioxide closing the mass balance within $\pm 10\%$. The associated error for the conversion values is $\pm 5\%$.

3. Results and discussion

3.1. Morphological phase diagram

Transmission electron microscopy (TEM) images of samples synthesized at different temperatures (between 70 °C and 180 °C) and a range of NaOH concentrations (from 1 to 15 M) for 10 h of hydrothermal treatment were used to determine the morphological phase diagram (Fig. 1). The phase boundaries were estimated taking into consideration the relative concentration of different nanostructures at given conditions but they did not imply a sharp transition to a pure phase. At low temperatures ($< 100^\circ\text{C}$), no formation of nano-structured ceria is observed when the concentration of base is lower than 10 M. Under these conditions, nanoparticulated ceria is observed with dimensions $> 5 \text{ nm}$ (Fig. 2). Increasing

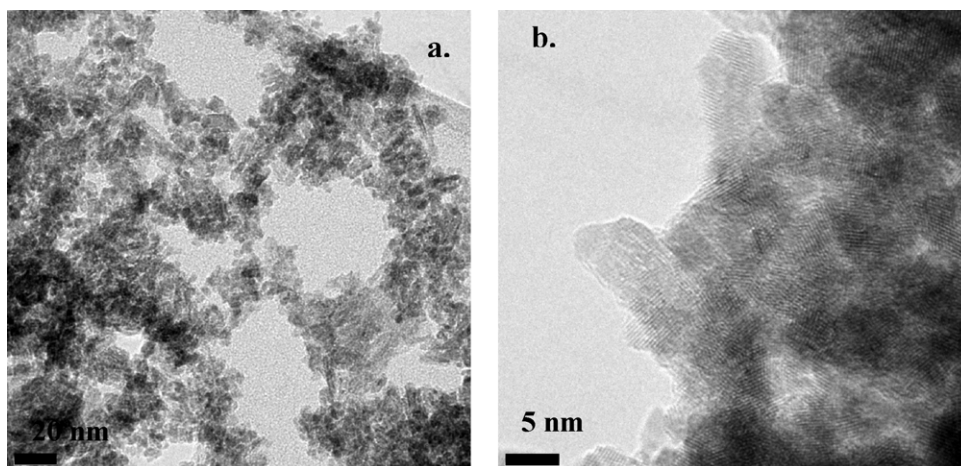


Fig. 2. TEM images of nanoparticulated ceria synthesized at 70 °C and 1 M NaOH.

the base concentration to >10 M at low temperatures (70 °C) results in the formation of 1D nanostructures with diameters of ~7 nm and lengths in the range of 20–80 nm with the simultaneous presence of nanoparticles.

The formation of nanorods (20–70 nm length) is observed even at low base concentrations of 1 M when the temperature is increased to 100 °C with a high presence of small particles (<5 nm). At a constant synthesis temperature of 100 °C, an increase in the base concentration leads to an increase in the concentration of the nanorods in detriment of the nanoparticles.

At a temperature of 150 °C, ceria nanorods are mainly formed over a wide range of base concentrations. At low NaOH concentrations (1 M), the co-presence of nanoparticulated ceria is observed. On the other hand, at high base concentrations (15 M), the formation of ceria nanocubes is observed. Increasing the hydrothermal temperature to 180 °C favours the formation of mainly nanocubes, although at low base concentration (<5 M), nanocubes co-exist with nanorods and nanoparticulated structures.

The diameter and length of the nanorods increases as the temperature and base concentration used during the hydrothermal syntheses increases. In this way, nanorods synthesized at 70 °C and a base concentration of 10 M show an average diameter of 7 nm and length in the range of 20–80 nm. Nanorods of 40–60 nm diameters and several micrometres length are formed at 150 °C and a NaOH concentration of 15 M (Fig. 3b).

In some of the samples synthesized under the studied conditions, a relatively small concentration of nanocrystals were observed surrounding the nanorods and/or nanocubes. These observations were in agreement with the established dissolution/recrystallization mechanism of formation of ceria nanostructures under hydrothermal methods [21,22]. At low temperature and low base concentration, the dissolution/recrystallization rate is slow, resulting in the formation of ceria nanoparticles from the anisotropic $\text{Ce}(\text{OH})_3$ nuclei initially formed in the solution.

When the temperature and/or base concentration are increased, the chemical potential to drive the anisotropic growth of the $\text{Ce}(\text{OH})_3$ nuclei is higher, forming ceria nanorods. At even higher temperatures and/or concentration of base, the $\text{Ce}(\text{OH})_3$ nuclei are oxidized into ceria with a nanocube morphology [9].

Representative samples of the three different ceria nanostructures (nanoparticles, nanorods and nanocubes) obtained under the studied range of hydrothermal conditions were further characterized. The hydrothermal conditions used for their synthesis are indicated with red circles in Fig. 1. Nanoparticulated ceria with dimensions >5 nm was synthesized by hydrothermal treatment at 70 °C and a base concentration (NaOH) of 1 M. Detailed TEM images of these nanoparticles are shown in Fig. 2 where the crystalline layers can easily be distinguished with enclosing (111) and (100) facets. Increasing the treatment temperature to 150 °C, ceria nanorods are mainly formed, independent of the base

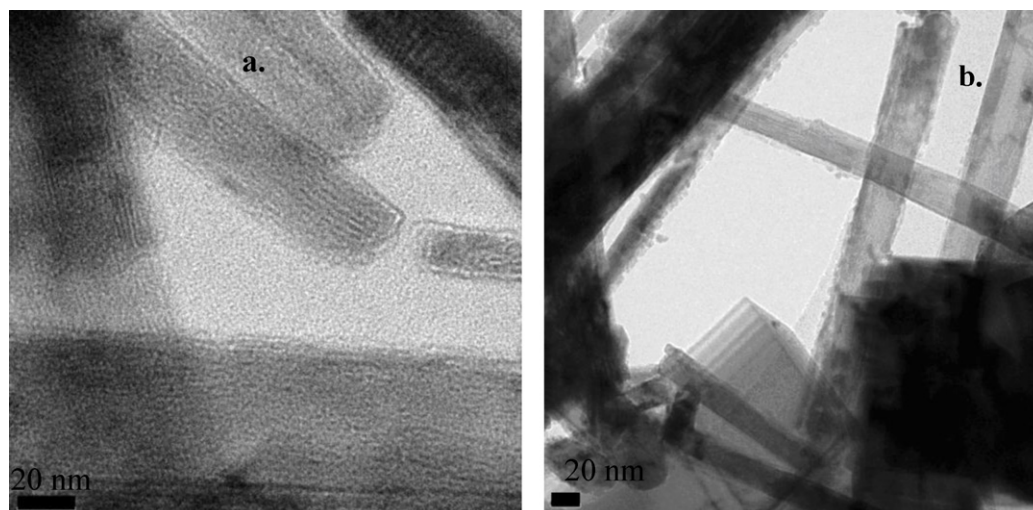


Fig. 3. TEM images of tubular structures synthesized at (a) 70 °C–15 M and (b) 150 °C–15 M.

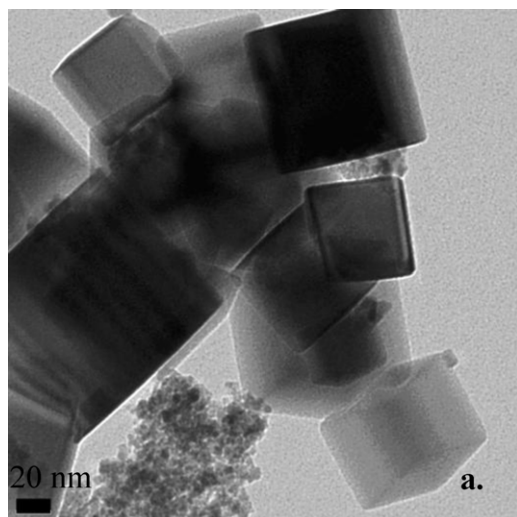


Fig. 4. TEM images of ceria nanocubes synthesized at 180 °C–15 M NaOH.

concentration within the studied range. Fig. 3 shows TEM images of nanorods synthesized under different hydrothermal conditions. Nanorods are formed of several parallel crystalline layers with enclosing (110) and (100) facets similar to the ones previously reported [15]. No evidence of hollow structures are observed as previously claimed for nanotubular structures synthesized by other methods [8]. Under certain conditions, monocrystal cylindrical nanostructures are surrounded by nanoparticles [15] as clearly shown in Fig. 3b. Finally, ceria nanocubes with enclosing (100) facets are formed at hydrothermal temperatures >180 °C with a variety of size lengths from 20 to 200 nm as shown in Fig. 4.

Nanoparticles, nanorods and nanocubes were analyzed by XRD (Fig. 5) revealing a crystalline structure with diffraction peaks at 2θ angles of 28.5°, 33.0°, 47.4°, 56.3°, 69.6° and 76.7° which corresponds to the (111), (200), (220), (311), (400) and (331) respectively of the crystalline planes of the pure cubic phase (ceria fluorite structure, JCPDS 34-0394). The mean crystallite size was determined using the Scherrer's equation [10]. For a given base concentration, the crystallite size increases as the temperature increases. The effect of the base concentration at a constant temperature on the crystallite size is though less crucial (Fig. 6). Samples synthesized at 70 °C show a mean crystallite size of ca.

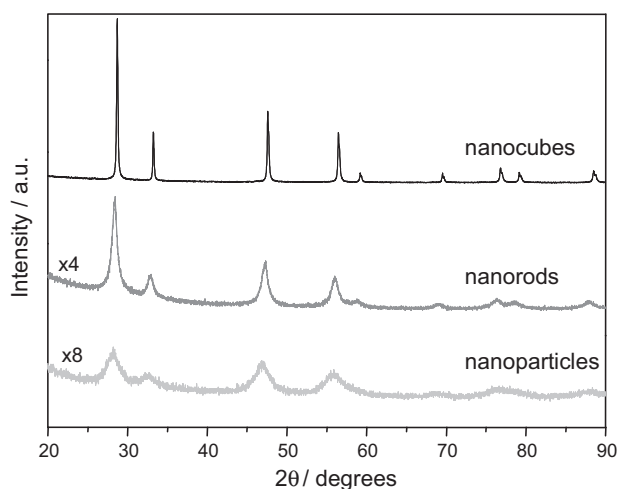


Fig. 5. XRD pattern of ceria nanoparticles (synthesized at 70 °C and 5 M NaOH), nanorods (synthesized at 100 °C and 15 M NaOH) and nanocubes (synthesized at 180 °C and 15 M NaOH).

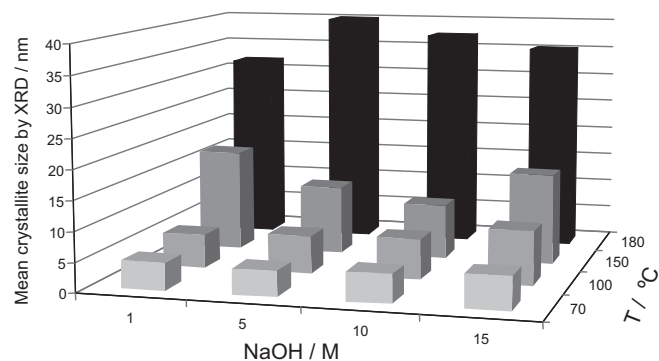


Fig. 6. Effect of temperature and NaOH concentration used during the preparation of the ceria catalysts on the mean particle size (calculated from the XRD spectra).

5 nm which corresponds to the nanoparticulated ceria observed by microscopy. By increasing the temperature for a constant base concentration, both the diameter and length of the nanorods increase. A further increase of the hydrothermal temperature leads to the formation of nanocubes with narrower XRD diffraction peaks indicating an increment of the mean crystallite size, up to 30–40 nm at 180 °C. These data are entirely consistent with the observations by microscopy discussed above. Similar tendencies were observed at all temperatures and base concentrations in the studied range.

3.2. Oxidation of naphthalene

The characterized representative samples of each morphology (particles, rods and cubes) were used in a catalytic study of the total oxidation of naphthalene. The conversion of the different ceria nanostructures with respect to temperature is shown in Fig. 7. CeO₂ nanoparticles showed the highest activity towards full oxidation followed by CeO₂ nanorods. Both catalysts were remarkably more active than CeO₂ nanocubes. All three catalysts showed 100% selectivity at conversions of about 20% and above. Below this conversion value, CO₂ remained the main product but small amounts of other products such as phenanthrene, naphthalene dione, dimethyl phthalate, benzene, alkyl benzenes, benzaldehyde, toluene and xylenes were also identified. The selectivity to CO₂ increased with the naphthalene conversion; this trend was similar for all these catalysts independently of the reaction temperature at which high

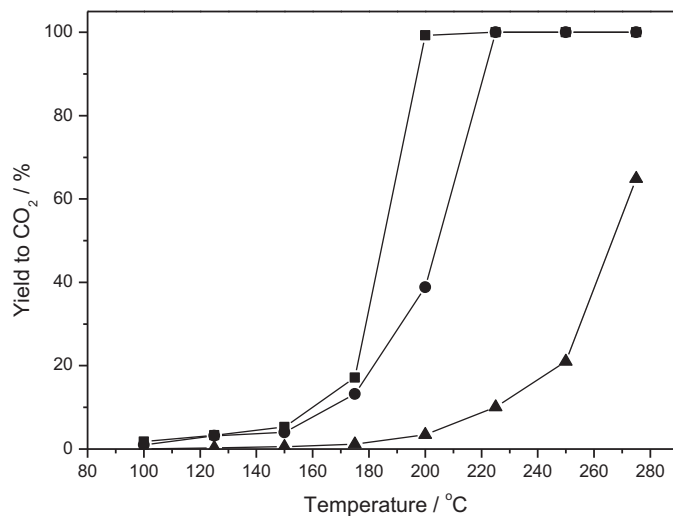


Fig. 7. Np total oxidation activity as a function of temperature of nanostructured ceria catalysts: (■) nanoparticles (5 M NaOH, 70 °C); (●) nanorods (15 M NaOH, 100 °C) and; (▲) nanocubes (15 M NaOH, 180 °C).

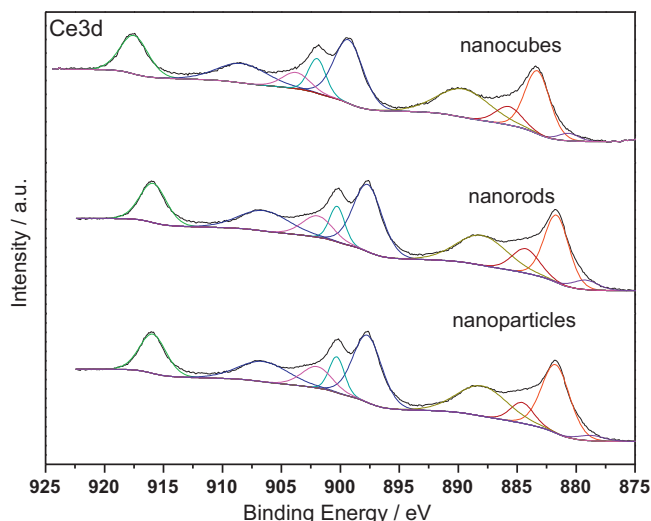


Fig. 8. Ce3d XPS spectra of CeO₂ nanostructured catalysts.

conversions were reached. Thus, the morphology does not seem to have an influence on the selectivity to CO₂, but it does strongly influence catalyst activity.

A catalytic activity of 90% conversion to carbon dioxide, using a space velocity of 25,000 h⁻¹ was achieved at only 190 °C with the ceria nanoparticles, which is amongst the best ceria catalysts reported in the literature to date [16,19,23–26]. This high activity is believed to be related to the high surface area and small crystallite size of the nanoparticles, as previously reported in the literature [16,19,20]. Accordingly, a decrease in activity is observed as the surface area decreases and the crystalline size increases from ceria nanoparticles to nanorods and nanocubes. On the other hand, if one considers the catalytic activity of the different ceria nano-morphologies per unit of surface area (Table 1), a different reactivity trend is drawn, the most active morphology being nanorods, followed by nanocubes and finally nanoparticles. Low levels of conversion (<20%) are considered for this comparison to avoid potential mass transfer limitations in low surface area catalysts.

XPS analyses were used to investigate surface oxidation states of the different ceria nanostructures. Fig. 8 shows the XPS spectra of Ce3d. It can be seen that no appreciable major differences between catalysts were observed. Two principal peaks of Ce3d_{5/2} and Ce3d_{3/2}, and four satellite peaks resulting from ionization attributed to Ce(IV) can be observed at 881.7, 888.4, 897.8, 900.3, 906.5 and 916.1 eV. A shift towards higher values occurs in the case of ceria nanocubes, likely to be due to the presence of more labile Ce⁴⁺–O bonds on the ceria surface. Thus, it can be concluded that the main valence of surface cerium was Ce⁴⁺ [27], albeit the existence of a low percentage of Ce³⁺ cannot be ruled out due to the presence of three small peaks at 878.5, 885 and 903.0 eV [28]. Again a shift to higher values was observed in the case of ceria nanocubes. Although it is possible in theory to determine the surface ratio of Ce³⁺ and Ce⁴⁺, in practice it can be difficult to achieve, as effects such as charging and line broadening make the amounts of both oxidation states difficult to quantify. Nevertheless, the amount of Ce³⁺ was tentatively calculated from the XPS spectra of Ce3d (Fig. 8) according to published methods [29] (see Table 2). All the samples analyzed contained predominantly surface Ce⁴⁺ with different amounts of Ce³⁺ depending on their morphology; ceria nanorods contained a higher amount of Ce³⁺ (16.4%) followed by ceria nanocubes (13.9%), being the lowest amount of Ce³⁺ for ceria nanoparticles (13.6%). The presence of higher amounts of surface

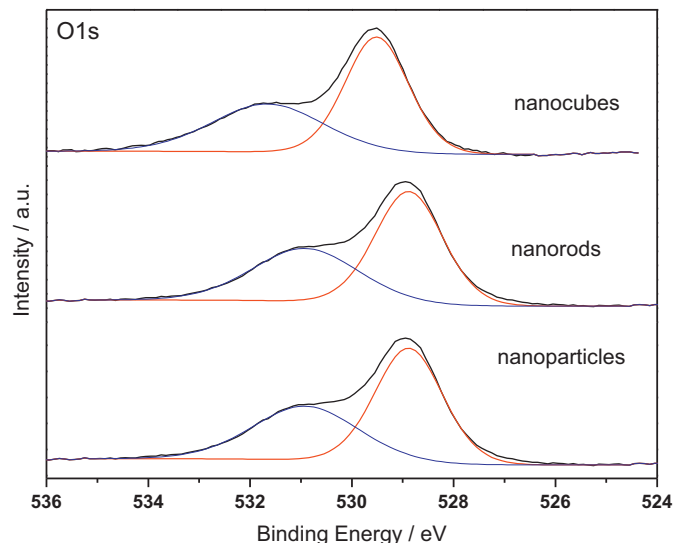


Fig. 9. O1s XPS spectra of CeO₂ nanostructured catalysts.

Ce³⁺ could probably be related to a higher presence of surface oxygen defects as previously reported in the literature [30].

XPS studies concentrating on oxygen species were also conducted (see Fig. 9). In the case of photoemission from oxygen, the O1s signal clearly shows two different surface oxygen species. The low binding energy peak (O_α: 529.0–530.5 eV) is ascribed to lattice oxygen whereas the high binding energy peak (O_β: 531.0–532.8 eV) is assigned to oxygen vacancies but also to surface adsorbed oxygen, hydroxyl, and carbonate groups [31]. Despite this, the XPS O_β/O_α ratio is a common way to roughly assess the amount of oxygen vacancies in the different ceria samples. As seen in Table 2, ceria nanorods present the highest O_β/O_α ratio and the lowest is obtained in the case of the nanoparticles. Summarizing, similar conclusions can be drawn from Ce3d and O1s XPS analyses; the concentration of surface oxygen vacancies decreases from ceria nanorods < nanocubes < nanoparticles. The same trend was observed in the catalytic activity per surface area of these nanostructures for the naphthalene oxidation, highlighting the importance of the amount of oxygen defects on the catalytic activity of ceria [32].

Complementary data can be drawn from the Raman analyses of the different CeO₂ nanostructured. A similar spectra is obtained for the three different morphologies (see Fig. 10) showing a single dominant band centred at a frequency of 462 cm⁻¹, characteristic of the CeO₂ vibrations. Table 2 summarizes the full width at half maximum (FWHM) of the main Raman band. Some authors [33] have associated the increase of the FWHM with a decrease in the crystallite size and/or a higher concentration of oxygen vacancies of the CeO₂. Nanocubes present the lowest width but also the highest particle size. Therefore the comparison of the amount of oxygen vacancies in the nanocubes with that of the other two ceria catalysts (nanorods and nanoparticles) is not straightforward. However, if nanorods and nanoparticles are compared some information can be attained. The FWHM in nanorods is marginally higher than in the nanoparticles in spite of the higher crystallite size of nanorods. These observations suggest that out of the three morphologies studies, the amount of oxygen vacancies is higher for the nanorods [34–36]. It must be indicated that the internal strain can also contribute to a higher width of this band. Raman results are also in agreement with the results obtained by XPS and with some previous works [37,38].

The variation on the concentration of surface oxygen defects on the different ceria nano-morphologies is believed to be related to

Table 1
Nanostructured ceria catalysts for total oxidation of naphthalene.

Catalyst	$T_{10\%}$ (°C)	$T_{50\%}$ (°C)	Formation rate of product @ 175 °C		
			g CO ₂ /kg cat h	g CO ₂ /m ² h × 10 ⁵	(g CO ₂ /m ² h × 10 ⁵)/(O _B /O _α)
CeO ₂ -np	155	180	42.3	29.4	21.2
CeO ₂ -nr	165	210	31.9	43.1	34.0
CeO ₂ -nc	225	270	2.85	38.5	29.6

T_{10} and T_{50} are the reaction temperatures required for yields to CO₂ of 10 and 50%, respectively.

Table 2
Characterization results of surface atomic values determined by XPS and FWHM determined by Raman.

Catalyst	CeO ₂ size ^a	S_{BET} (m ² /g)	Surface Ce ³⁺ (at.%) ^b	O _α (at.%)	O _β ^b (at.%)	O _β /O _α ^b	FWHM ^c (cm ⁻¹)
CeO ₂ -np	4.5	144	13.6	58.0	42.0	0.72	60
CeO ₂ -nr	9.1	74	16.4	55.8	44.2	0.79	62
CeO ₂ -nc	37.3	13	13.9	56.4	43.6	0.77	12

^a Determined by XRD analysis using the Scherrer's equation.

^b Determined by XPS analysis.

^c Determined by Raman analysis.

the crystalline layers selectively exposed in each structure. Thus, higher catalytic activities per unit of surface area are observed on the surface of CeO₂ nanorods and nanocubes with enclosing (1 1 0) and (1 0 0) facets and (1 0 0) facets, respectively. Additionally it can be seen that the position of the O_α binding energy differs depending on the morphology since O_α binding energies corresponding to ceria nanocubes are shifted to higher values. This fact could be related to a higher mobility of the lattice oxygen in the case of ceria nanocubes with enclosing (1 0 0) facets as it has been previously reported [39]. On the other hand, the (1 1 1) planes exposed on the nanoparticles presented the lowest catalytic activity per unit surface area for the full oxidation of naphthalene. These data are in agreement to molecular simulation results. Computer modelling showed that the low-index (1 1 1) surface has the lowest surface energy and is thus the most stable surface [40]. Similarly Conesa et al. [41] indicated that less energy is required to form oxygen vacancies on (1 1 0) and (1 0 0) than on (1 1 1).

The link between exposed planes and the catalytic performance of ceria for the oxidation polycyclic aromatic hydrocarbons such as naphthalene has not been experimentally reported yet. However, the influence of the exposed planes on the catalytic performance for the oxidation of CO has been widely studied being in agreement

with the observations of this study for the oxidation of polycyclic aromatic hydrocarbons. According to Tana et al. [42], the CeO₂ nanoparticles mainly expose the stable (1 1 1) plane on the surface, whereas the rod-shaped nanostructures preferentially expose the reactive (1 1 0) and (1 0 0) planes, giving higher oxygen storage capacity and catalytic activity for CO oxidation. In another work Zhou et al. [43], showed that CeO₂ nanorods with well-defined reactive planes ((0 0 1) and (1 1 0)) show higher CO oxidation activity than CeO₂ nanoparticles because of their more reactive planes.

4. Conclusions

A morphology phase diagram showing different ceria nanostructures (particles, rods and cubes) has been established by studying the effect of temperature and base concentration under hydrothermal conditions. One representative sample of each of these three nanostructures has been tested as catalyst in the total oxidation of naphthalene. Ceria nanoparticles are the most active of these structures due to their high surface area and low crystalline size with comparative activity to the best reported in the literature to date. However if the catalytic activity is normalized by the unit of surface area, nanorods (with (1 1 0) and (1 0 0) as preferential planes) are the most active catalyst followed by nanocubes ((1 0 0) as the main exposed plane), with nanoparticles (with (1 1 1) as the preferential plane) presenting the lowest areal rate. This observed trend is directly related to the Ce³⁺/Ce⁴⁺ ratio and concentration of surface oxygen vacancies as shown by the XPS and Raman analyses, respectively. These results support previous works that propose that (1 1 0) and (1 0 0) planes are more reactive than (1 1 1) planes, giving higher oxygen storage capacity and consequently a higher oxidation catalytic activity.

Acknowledgements

We thank EPSRC (UK) and the Ministry of Science and Innovation (Spain) and Plan E through project ENE2009-11353 for funding.

References

- [1] M. Mogensen, N.M. Sammes, G.A. Tompsett, *Solid State Ionics* 129 (2000) 63–94.
- [2] W. Lai, S.M. Haile, *Journal of the American Chemical Society* 88 (2005) 2979–2997.
- [3] S. Saitzek, F. Guinneton, L. Sauques, K. Aguir, J.R. Gavarri, *Optical Materials* 30 (2007) 407–415.
- [4] M. Godickemeier, K. Sasaki, L.J. Gauckler, I. Riess, *Journal of Electrochemical Society* 144 (1997) 1635–1646.
- [5] J. Kaspar, P. Fornasiero, M. Graziani, *Catalysis Today* 50 (1999) 285–298.
- [6] P. Singh, M.S. Hedge, *Journal of Solid State Chemistry* 181 (2008) 3248–3256.

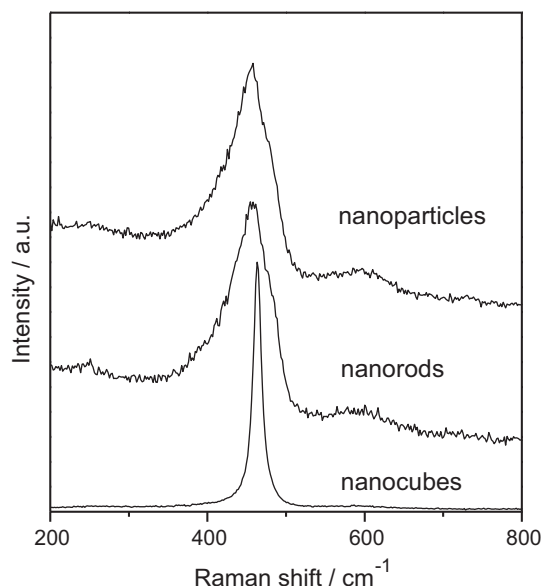


Fig. 10. Raman spectra corresponding to different CeO₂ nanostructures.

- [7] D.C. Sayle, S.A. Maicaneanu, G.W. Watson, *Journal of the American Chemical Society* 124 (2002) 11429–11439.
- [8] L. Gonzalez-Rovira, J.M. Sanchez-Amaya, M. Lopez-Haro, E. del Rio, A.B. Hungria, P. Midgley, J.J. Calvino, S. Bernal, F.J. Botana, *Nano Letters* 9 (2009) 1395–1400.
- [9] H.-X. Mai, L.-D. Sun, Y.-W. Zhang, R. Si, W. Feng, H.-P. Zhang, H.-C. Liu, C.-H. Yan, *The Journal of Physical Chemistry B* 109 (2005) 24380–24385.
- [10] S. Wang, J. Zhang, J. Jiang, R. Liu, B. Zhu, M. Xu, Y. Wang, J. Cao, M. Li, Z. Yuan, S. Zhang, W. Huang, S. Wu, *Microporous and Mesoporous Materials* 123 (2009) 349–353.
- [11] I. Yamaguchi, M. Watanabe, T. Shinagawa, M. Chigane, M. Inaba, A. Tasaka, M. Izaki, *ACS Applied Materials and Interfaces* 1 (2009) 1070–1075.
- [12] Z.L. Liu, B. Guo, L. Hong, H.X. Jiang, *Journal of Physics and Chemistry of Solids* 66 (2005) 161–167.
- [13] W.-Q. Han, L. Wu, Y. Zhu, *Journal of the American Chemical Society* 127 (2005) 12814–12815.
- [14] L. Yan, R. Yu, J. Chen, X. Xing, *Crystal Growth and Design* 8 (2008) 1474–1477.
- [15] G. Chen, C. Xu, X. Song, W. Zhao, Y. Ding, S. Sun, *Inorganic Chemistry* 47 (2008) 723–728.
- [16] T. Garcia, B. Solsona, S.H. Taylor, *Applied Catalysis B: Environmental* 66 (2006) 92–99.
- [17] P.H. McMurry, *Atmospheric Environment* 34 (2000) 1959–1999.
- [18] J.L. Shie, C.Y. Chang, J.H. Chen, W.T. Tsai, Y.H. Chen, C.S. Chiou, C.F. Chang, *Applied Catalysis B: Environmental* 58 (2005) 289–297.
- [19] T. Garcia, B. Solsona, S.H. Taylor, *Catalysis Letters* 105 (2005) 183–189.
- [20] A. Aranda, J.M. Lopez, R. Murillo, A.M. Mastral, A. Dejoz, I. Vazquez, B. Solsona, S.H. Taylor, T. Garcia, *Journal of Hazardous Materials* 171 (2009) 393–399.
- [21] M. Hirano, E. Kato, *Journal of the American Ceramic Society* 82 (1999) 786–788.
- [22] Q. Wu, F. Zhang, P. Xiao, H. Tao, X. Wang, Z. Hu, Y. Li, *Journal of Physical Chemistry C* 112 (2008) 17076–17080.
- [23] B. Puertolas, B. Solsona, S. Agouram, R. Murillo, A.M. Mastral, A. Aranda, S.H. Taylor, T. Garcia, *Applied Catalysis B: Environmental* 93 (2010) 395–405.
- [24] X.W. Zhang, S.C. Shen, L.E. Yu, S. Kawi, K. Hidajat, K.Y.S. Ng, *Applied Catalysis A: General* 250 (2003) 341–352.
- [25] J. Carno, M. Berg, S. Jaras, *Fuel* 75 (1996) 959–965.
- [26] A. Bampenrat, V. Meeyoo, B. Kitiyanan, P. Rangsunvigit, T. Rirksomboon, *Catalysis Communications* 9 (2008) 2349–2352.
- [27] H.B. Zou, X.F. Dong, W.M. Lin, *Applied Surface Science* 253 (2006) 2893–2898.
- [28] B. Shanghong, W. Xue, L. Xiaoyan, J. Yuan, *Rare Earths* 24 (2006) 177–181.
- [29] A. Fujimori, *Physical Review B* 28 (1983) 2281–2283.
- [30] T. Naganuma, E. Traversa, *Nanoscale* 4 (2012) 4950–4953.
- [31] A. Galtayries, R. Sporken, J. Riga, G. Blanchard, R. Caudano, *Journal of Electron Spectroscopy and Related Phenomena* 88 (1998) 951–956.
- [32] E.N. Ntainjua, T.E. Davies, T. Garcia, B. Solsona, S.H. Taylor, *Catalysis Letters* 141 (2011) 1732–1738.
- [33] E.N. Ndifor, T. Garcia, B. Solsona, S.H. Taylor, *Applied Catalysis B: Environmental* 76 (2007) 248–256.
- [34] I. Kosacki, T. Suzuki, H.U. Anderson, P. Colomban, *Solid State Ionics* 149 (2002) 99–105.
- [35] L.A. Falkovsky, J. Camassel, *Physica B* 284 (2000) 1145–1146.
- [36] J.E. Spanier, R.D. Robinson, F. Zheng, S.W. Chan, I.P. Herman, *Physical Review B* 64 (2001).
- [37] N.J. Lawrence, J.R. Brewer, L. Wang, T.S. Wu, J. Wells-Kingsbury, M.M. Ihrig, G.H. Wang, Y.L. Soo, W.N. Mei, C.L. Cheung, *Nano Letters* 11 (2011) 2666–2671.
- [38] Y. Lee, G.H. He, A.J. Akey, R. Si, M. Flytzani-Stephanopoulos, I.P. Herman, *Journal of the American Chemical Society* 133 (2011) 12952–12955.
- [39] Z.Q. Yang, K.B. Zhou, X.W. Liu, Q. Tian, D.Y. Lu, S. Yang, *Nanotechnology* 18 (2007).
- [40] T.X.T. Sayle, S.C. Parker, C.R.A. Catlow, *Journal of the Chemical Society: Chemical Communications* (1992) 977–978.
- [41] D. Gamarra, G. Munuera, A.B. Hungria, M. Fernandez-Garcia, J.C. Conesa, P.A. Midgley, X.Q. Wang, J.C. Hanson, J.A. Rodriguez, A. Martinez-Arias, *Journal of Physical Chemistry C* 111 (2007) 11026–11038.
- [42] Tana, M.L. Zhang, J. Li, H.J. Li, Y. Li, W.J. Shen, *Catalysis Today* 148 (2009) 179–183.
- [43] K.B. Zhou, X. Wang, X.M. Sun, Q. Peng, Y.D. Li, *Journal of Catalysis* 229 (2005) 206–212.